

Measurement of ultra-high-energy diffuse gamma-ray emission of the Galactic plane from 10 TeV to 1 PeV with LHAASO-KM2A

Zhen Cao,^{1,2,3} F. Aharonian,^{4,5} Q. An,^{6,7} Axikegu,⁸ Y.X. Bai,^{1,3} Y.W. Bao,⁹ D. Bastieri,¹⁰ X.J. Bi,^{1,2,3} Y.J. Bi,^{1,3} J.T. Cai,¹⁰ Q. Cao,¹¹ W.Y. Cao,⁷ Zhe Cao,^{6,7} J. Chang,¹² J.F. Chang,^{1,3,6} A.M. Chen,¹³ E.S. Chen,^{1,2,3} Liang Chen,¹⁴ Lin Chen,⁸ Long Chen,⁸ M.J. Chen,^{1,3} M.L. Chen,^{1,3,6} Q.H. Chen,⁸ S.H. Chen,^{1,2,3} S.Z. Chen,^{1,3} T.L. Chen,¹⁵ Y. Chen,⁹ N. Cheng,^{1,3} Y.D. Cheng,^{1,3} M.Y. Cui,¹² S.W. Cui,¹¹ X.H. Cui,¹⁶ Y.D. Cui,¹⁷ B.Z. Dai,¹⁸ H.L. Dai,^{1,3,6} Z.G. Dai,⁷ Danzengluobu,¹⁵ D. della Volpe,¹⁹ X.Q. Dong,^{1,2,3} K.K. Duan,¹² J.H. Fan,¹⁰ Y.Z. Fan,¹² J. Fang,¹⁸ K. Fang,^{1,3} C.F. Feng,²⁰ L. Feng,¹² S.H. Feng,^{1,3} X.T. Feng,²⁰ Y.L. Feng,¹⁵ S. Gabici,²¹ B. Gao,^{1,3} C.D. Gao,²⁰ L.Q. Gao,^{1,2,3} Q. Gao,¹⁵ W. Gao,^{1,3} W.K. Gao,^{1,2,3} M.M. Ge,¹⁸ L.S. Geng,^{1,3} G. Giacinti,¹³ G.H. Gong,²² Q.B. Gou,^{1,3} M.H. Gu,^{1,3,6} F.L. Guo,¹⁴ X.L. Guo,⁸ Y.Q. Guo,^{1,3} Y.Y. Guo,¹² Y.A. Han,²³ H.H. He,^{1,2,3} H.N. He,¹² J.Y. He,¹² X.B. He,¹⁷ Y. He,⁸ M. Heller,¹⁹ Y.K. Hor,¹⁷ B.W. Hou,^{1,2,3} C. Hou,^{1,3} X. Hou,²⁴ H.B. Hu,^{1,2,3} Q. Hu,^{7,12} S.C. Hu,^{1,2,3} D.H. Huang,⁸ T.Q. Huang,^{1,3} W.J. Huang,¹⁷ X.T. Huang,²⁰ X.Y. Huang,¹² Y. Huang,^{1,2,3} Z.C. Huang,⁸ X.L. Ji,^{1,3,6} H.Y. Jia,⁸ K. Jia,²⁰ K. Jiang,^{6,7} X.W. Jiang,^{1,3} Z.J. Jiang,¹⁸ M. Jin,⁸ M.M. Kang,²⁵ T. Ke,^{1,3} D. Kuleshov,²⁶ K. Kurinov,²⁶ B.B. Li,¹¹ Cheng Li,^{6,7} Cong Li,^{1,3} D. Li,^{1,2,3} F. Li,^{1,3,6} H.B. Li,^{1,3} H.C. Li,^{1,3} H.Y. Li,^{7,12} J. Li,^{7,12} Jian Li,⁷ Jie Li,^{1,3,6} K. Li,^{1,3} W.L. Li,²⁰ W.L. Li,¹³ X.R. Li,^{1,3} Xin Li,^{6,7} Y.Z. Li,^{1,2,3} Zhe Li,^{1,3} Zhuo Li,²⁷ E.W. Liang,²⁸ Y.F. Liang,²⁸ S.J. Lin,¹⁷ B. Liu,⁷ C. Liu,^{1,3} D. Liu,²⁰ H. Liu,⁸ H.D. Liu,²³ J. Liu,^{1,3} J.L. Liu,^{1,3} J.Y. Liu,^{1,3} M.Y. Liu,¹⁵ R.Y. Liu,⁹ S.M. Liu,⁸ W. Liu,^{1,3} Y. Liu,¹⁰ Y.N. Liu,²² R. Lu,¹⁸ Q. Luo,¹⁷ H.K. Lv,^{1,3} B.Q. Ma,²⁷ L.L. Ma,^{1,3} X.H. Ma,^{1,3} J.R. Mao,²⁴ Z. Min,^{1,3} W. Mitthumsiri,²⁹ H.J. Mu,²³ Y.C. Nan,^{1,3} A. Neronov,²¹ Z.W. Ou,¹⁷ B.Y. Pang,⁸ P. Pattarakijwanich,²⁹ Z.Y. Pei,¹⁰ M.Y. Qi,^{1,3} Y.Q. Qi,¹¹ B.Q. Qiao,^{1,3} J.J. Qin,⁷ D. Ruffolo,²⁹ A. Sáiz,²⁹ D. Semikoz,²¹ C.Y. Shao,¹⁷ L. Shao,¹¹ O. Shchegolev,^{26,30} X.D. Sheng,^{1,3} F.W. Shu,³¹ H.C. Song,²⁷ Yu.V. Stenkin,^{26,30} V. Stepanov,²⁶ Y. Su,¹² Q.N. Sun,⁸ X.N. Sun,²⁸ Z.B. Sun,³² P.H.T. Tam,¹⁷ Q.W. Tang,³¹ Z.B. Tang,^{6,7} W.W. Tian,^{2,16} C. Wang,³² C.B. Wang,⁸ G.W. Wang,⁷ H.G. Wang,¹⁰ H.H. Wang,¹⁷ J.C. Wang,²⁴ K. Wang,⁹ L.P. Wang,²⁰ L.Y. Wang,^{1,3} P.H. Wang,⁸ R. Wang,²⁰ W. Wang,¹⁷ X.G. Wang,²⁸ X.Y. Wang,⁹ Y. Wang,⁸ Y.D. Wang,^{1,3} Y.J. Wang,^{1,3} Z.H. Wang,²⁵ Z.X. Wang,¹⁸ Zhen Wang,¹³ Zheng Wang,^{1,3,6} D.M. Wei,¹² J.J. Wei,¹² Y.J. Wei,^{1,2,3} T. Wen,¹⁸ C.Y. Wu,^{1,3} H.R. Wu,^{1,3} S. Wu,^{1,3} X.F. Wu,¹² Y.S. Wu,⁷ S.Q. Xi,^{1,3} J. Xia,^{7,12} J.J. Xia,⁸ G.M. Xiang,^{2,14} D.X. Xiao,¹¹ G. Xiao,^{1,3} G.G. Xin,^{1,3} Y.L. Xin,⁸ Y. Xing,¹⁴ Z. Xiong,^{1,2,3} D.L. Xu,¹³ R.F. Xu,^{1,2,3} R.X. Xu,²⁷ W.L. Xu,²⁵ L. Xue,²⁰ D.H. Yan,¹⁸ J.Z. Yan,¹² T. Yan,^{1,3} C.W. Yang,²⁵ F. Yang,¹¹ F.F. Yang,^{1,3,6} H.W. Yang,¹⁷ J.Y. Yang,¹⁷ L.L. Yang,¹⁷ M.J. Yang,^{1,3} R.Z. Yang,⁷ S.B. Yang,¹⁸ Y.H. Yao,²⁵ Z.G. Yao,^{1,3} Y.M. Ye,²² L.Q. Yin,^{1,3} N. Yin,²⁰ X.H. You,^{1,3} Z.Y. You,^{1,2,3} Y.H. Yu,⁷ Q. Yuan,¹² H. Yue,^{1,2,3} H.D. Zeng,¹² T.X. Zeng,^{1,3,6} W. Zeng,¹⁸ M. Zha,^{1,3} B.B. Zhang,⁹ F. Zhang,⁸ H.M. Zhang,⁹ H.Y. Zhang,^{1,3} J.L. Zhang,¹⁶ L.X. Zhang,¹⁰ Li Zhang,¹⁸ P.F. Zhang,¹⁸ P.P. Zhang,^{7,12} R. Zhang,^{7,12} S.B. Zhang,^{2,16} S.R. Zhang,¹¹ S.S. Zhang,^{1,3} X. Zhang,⁹ X.P. Zhang,^{1,3} Y.F. Zhang,⁸ Yi Zhang,^{1,12} Yong Zhang,^{1,3} B. Zhao,⁸ J. Zhao,^{1,3} L. Zhao,^{6,7} L.Z. Zhao,¹¹ S.P. Zhao,^{12,20} F. Zheng,³² B. Zhou,^{1,3} H. Zhou,¹³ J.N. Zhou,¹⁴ M. Zhou,³¹ P. Zhou,⁹ R. Zhou,²⁵ X.X. Zhou,⁸ C.G. Zhu,²⁰ F.R. Zhu,⁸ H. Zhu,¹⁶ K.J. Zhu,^{1,2,3,6} and X. Zuo^{1,3}

(The LHAASO Collaboration)*

¹Key Laboratory of Particle Astrophysics & Experimental Physics Division & Computing Center, Institute of High Energy Physics, Chinese Academy of Sciences, 100049 Beijing, China

²University of Chinese Academy of Sciences, 100049 Beijing, China

³Tianfu Cosmic Ray Research Center, 610000 Chengdu, Sichuan, China

⁴Dublin Institute for Advanced Studies, 31 Fitzwilliam Place, 2 Dublin, Ireland

⁵Max-Planck-Institut für Kernphysik, P.O. Box 103980, 69029 Heidelberg, Germany

⁶State Key Laboratory of Particle Detection and Electronics, China

⁷University of Science and Technology of China, 230026 Hefei, Anhui, China

⁸School of Physical Science and Technology & School of Information Science and Technology, Southwest Jiaotong University, 610031 Chengdu, Sichuan, China

⁹School of Astronomy and Space Science, Nanjing University, 210023 Nanjing, Jiangsu, China

¹⁰Center for Astrophysics, Guangzhou University, 510006 Guangzhou, Guangdong, China

¹¹Hebei Normal University, 050024 Shijiazhuang, Hebei, China

¹²Key Laboratory of Dark Matter and Space Astronomy & Key Laboratory of Radio Astronomy, Purple Mountain Observatory, Chinese Academy of Sciences, 210023 Nanjing, Jiangsu, China

¹³Tsung-Dao Lee Institute & School of Physics and Astronomy,

Shanghai Jiao Tong University, 200240 Shanghai, China

¹⁴Key Laboratory for Research in Galaxies and Cosmology,

Shanghai Astronomical Observatory, Chinese Academy of Sciences, 200030 Shanghai, China

¹⁵Key Laboratory of Cosmic Rays (Tibet University), Ministry of Education, 850000 Lhasa, Tibet, China

¹⁶National Astronomical Observatories, Chinese Academy of Sciences, 100101 Beijing, China

¹⁷School of Physics and Astronomy (Zhuhai) & School of Physics (Guangzhou)

& Sino-French Institute of Nuclear Engineering and Technology (Zhuhai),

Sun Yat-sen University, 519000 Zhuhai & 510275 Guangzhou, Guangdong, China

¹⁸*School of Physics and Astronomy, Yunnan University, 650091 Kunming, Yunnan, China*

¹⁹*Département de Physique Nucléaire et Corpusculaire, Faculté de Sciences,
Université de Genève, 24 Quai Ernest Ansermet, 1211 Geneva, Switzerland*

²⁰*Institute of Frontier and Interdisciplinary Science, Shandong University, 266237 Qingdao, Shandong, China*

²¹*APC, Université Paris Cité, CNRS/IN2P3, CEA/IRFU, Observatoire de Paris, 119 75205 Paris, France*

²²*Department of Engineering Physics, Tsinghua University, 100084 Beijing, China*

²³*School of Physics and Microelectronics, Zhengzhou University, 450001 Zhengzhou, Henan, China*

²⁴*Yunnan Observatories, Chinese Academy of Sciences, 650216 Kunming, Yunnan, China*

²⁵*College of Physics, Sichuan University, 610065 Chengdu, Sichuan, China*

²⁶*Institute for Nuclear Research of Russian Academy of Sciences, 117312 Moscow, Russia*

²⁷*School of Physics, Peking University, 100871 Beijing, China*

²⁸*School of Physical Science and Technology, Guangxi University, 530004 Nanning, Guangxi, China*

²⁹*Department of Physics, Faculty of Science, Mahidol University, 10400 Bangkok, Thailand*

³⁰*Moscow Institute of Physics and Technology, 141700 Moscow, Russia*

³¹*Center for Relativistic Astrophysics and High Energy Physics,*

*School of Physics and Materials Science & Institute of Space Science and Technology,
Nanchang University, 330031 Nanchang, Jiangxi, China*

³²*National Space Science Center, Chinese Academy of Sciences, 100190 Beijing, China*

(Dated: August 22, 2023)

The diffuse Galactic γ -ray emission, mainly produced via interactions between cosmic rays and the interstellar medium and/or radiation field, is a very important probe of the distribution, propagation, and interaction of cosmic rays in the Milky Way. In this work we report the measurements of diffuse γ -rays from the Galactic plane between 10 TeV and 1 PeV energies, with the square kilometer array of the Large High Altitude Air Shower Observatory (LHAASO). Diffuse emissions from the inner ($15^\circ < l < 125^\circ$, $|b| < 5^\circ$) and outer ($125^\circ < l < 235^\circ$, $|b| < 5^\circ$) Galactic plane are detected with 29.1σ and 12.7σ significance, respectively. The outer Galactic plane diffuse emission is detected for the first time in the very- to ultra-high-energy domain ($E > 10$ TeV). The energy spectrum in the inner Galaxy regions can be described by a power-law function with an index of -2.99 ± 0.04 , which is different from the curved spectrum as expected from hadronic interactions between locally measured cosmic rays and the line-of-sight integrated gas content. Furthermore, the measured flux is higher by a factor of ~ 3 than the prediction. A similar spectrum with an index of -2.99 ± 0.07 is found in the outer Galaxy region, and the absolute flux for $10 \lesssim E \lesssim 60$ TeV is again higher than the prediction for hadronic cosmic ray interactions. The latitude distributions of the diffuse emission are consistent with the gas distribution, while the longitude distributions show clear deviation from the gas distribution. The LHAASO measurements imply that either additional emission sources exist or cosmic ray intensities have spatial variations.

PACS numbers: 95.85.Pw, 98.70.Sa

The origin and propagation of cosmic rays (CRs) remain among the most important unresolved problems in astrophysics. Unlike the direct measurements of energy spectra and anisotropies of CRs in the local vicinity, the diffuse Galactic γ -ray emission allows a measurement of the spatial distribution of CRs throughout the Galaxy. It can thus provide much more important information of the production and propagation of CRs. Typically there are three main components of the diffuse Galactic emission [1–3]: the decay of neutral pions produced by inelastic collisions between CR nuclei and the interstellar medium (ISM), the inverse Compton scattering (ICS) of CR e^\pm off the interstellar radiation field (ISRF), and the bremsstrahlung radiation of e^\pm in the ISM. The canonical CR propagation and interaction model (homogeneous and isotropic diffusion) can largely account for the all-sky data measured by space telescopes while being consistent with the local CR measurements, except for the underpredicted γ -ray fluxes in the inner Galaxy for energies above a few GeV [2–4].

For energies below 1 TeV, the all-sky diffuse emission has been measured by space detectors such as OSO-3 [5], SAS-2 [6], COS-B [7], EGRET [8], and Fermi-LAT [4]. At higher energies, successful detections of the diffuse emission were only achieved by a few ground-based experiments in selected regions of the Galactic plane [9–14]. The recent measurements of the diffuse emission above 100 TeV by Tibet-AS γ [12] revealed flux excesses compared with the conventional model prediction (e.g., [15–17]). High-precision measurements of the diffuse emission in the very-high-energy (VHE; 30 GeV to 30 TeV [18]) to ultra-high-energy (UHE; 30 TeV to 30 PeV [18]) domain, with only minor statistical and systematic uncertainties, are crucial to understanding the origin and propagation of CRs, particularly the physical origin of the new spectral features of CR nuclei by recent direct measurements [19–22] and the potential contributions from unresolved source populations (e.g., [1, 18, 23–26]).

We report the measurements of the diffuse emission from the Galactic plane in a wide energy range, from 10 TeV to 1000 TeV. We use the data recorded by the square kilometer array (KM2A) of the Large High Altitude Air Shower Observatory (LHAASO) experiment located at Haizi Mountain ($100^\circ.01\text{E}$, $29^\circ.35\text{N}$; 4400 m above the sea level), Daocheng,

* E-mail: xyhuang@pmo.ac.cn; xisq@ihep.ac.cn; yuyh@ustc.edu.cn; yuanq@pmo.ac.cn; zhangrui@pmo.ac.cn; zhangyi@pmo.ac.cn; zhaosp@mail.sdu.edu.cn

Sichuan province, China [27]. The LHAASO experiment is a large area, wide field-of-view observatory for CRs and γ -rays with hybrid detection techniques [27]. In April 2019, LHAASO started taking data with a partial array, and successfully opened the PeV γ -ray window with its extraordinary sensitivity [28–32]. In July 2021, LHAASO completed the installation of its entire detector array and started its scientific operation.

Air showers produced by primary particles were simulated with the CORSIKA code (version 7.6400) [33], with the GHEISHA and QGSII models for low-energy (≤ 80 GeV) and high-energy (> 80 GeV) hadronic interactions. We simulate γ -ray events, with energies from 1 TeV to 10 PeV following a power-law spectrum of $E^{-2.0}$, with zenith angles from 0° to 70° , and with shower cores randomly distributed within 1 km from the array center. The detector response of KM2A was simulated using a specific software G4KM2A [34], which is based on the Geant4 framework (v4.10.00) [35]. The simulation data were reconstructed using the same algorithms applied to the experimental data. Comparisons between simulation and observational data show good consistency [36].

Data analysis. — The present work utilizes data acquired by the KM2A 1/2 array from December 26, 2019 to November 30, 2020 (with a live time of 302 days), by the 3/4 array from December 1, 2020 to July 19, 2021 (with a live time of 219 days), and by the full array from July 20, 2021 to September 30, 2022 (with a live time of 423 days). The whole Galactic plane with Galactic latitudes within $\pm 5^\circ$ in the field-of-view of LHAASO is adopted as our region of interest (ROI). We further divide the analysis region into two parts, the inner Galaxy region ($|b| < 5^\circ$, $15^\circ < l < 125^\circ$) and outer Galaxy region ($|b| < 5^\circ$, $125^\circ < l < 235^\circ$), for detailed studies.

We use the sequence of arrival times and deposited energy of the secondary particles recorded by the electromagnetic detectors (EDs) to reconstruct the direction and energy of a primary CR or γ -ray event. The 68% containment angle of KM2A is about $0.5^\circ - 0.8^\circ$ at 20 TeV and $0.24^\circ - 0.30^\circ$ at 100 TeV, depending on the zenith angles of incident photons [36]. The energy is reconstructed using the particle density at a perpendicular distance of 50 m from the shower axis, ρ_{50} , as obtained via a likelihood fit of the lateral distribution using the Nishimura-Kamata-Greisen (NKG; [37]) function. The energy resolution is about 24% at 20 TeV and 13% at 100 TeV, for events with zenith angles less than 20° [36].

The numbers of muons recorded by the muon detectors (MDs) were used to distinguish γ -ray-induced showers from CR-induced ones. The muon-to-electromagnetic-particle ratio, $R_{\mu e} = \log[(N_\mu + 10^{-4})/N_e]$, was used to reject CR events. For point-like source analysis, the muon selection criteria were optimized to guarantee retaining 90% of the γ -ray events at energies above 100 TeV for a typical Crab-like source based on simulations [36]. In this work, we restricted criteria to further suppress the CR background at high energies, thus obtaining a maximal detection significance of the diffuse emission. The CR rejection power is about 98% at 10 TeV and 99.9993% at 400 TeV, and the γ -ray survival fraction is higher than 50% for the interest energy range in this work.

We further apply the following event selection conditions:

- 1) the number of triggered EDs and the number of deposited particles used in the shower reconstruction are both larger than ten;
- 2) the zenith angle of the reconstructed direction is less than 50° ;
- 3) the number of particles detected within 40 m from the shower core is larger than that within 40 – 100 m;
- 4) the shower age is within 0.6 – 2.4.

The data are binned into $0.1^\circ \times 0.1^\circ$ pixels in celestial coordinates, and into equal logarithmic energy bins with bin width $\Delta \log E = 0.2$. Due to limited statistics in the outer Galaxy region, we use a bin width of $\Delta \log E = 0.4$.

In this study, the “direct integral method” [38] was utilized to estimate the background in each pixel. This approach assumes that the collecting efficiency’s spatial distribution in the detector coordinates remains stable over a short period. The background can be accurately determined by convolving the total event rate with the normalized spatial distribution. However, due to changes in detector efficiency of EDs caused by temperature variations, which differ for different detectors, the spatial distribution undergoes slight changes over time during the data taking. We employed a sliding window method to obtain a smoothed spatial distribution to address this issue. Specifically, a time step of 1 hour was selected, and at each step, events that arrive within ± 5 hours were used to calculate the spatial distribution. This long time window may result in spurious large-scale structures of the background, which need to be corrected during the analysis (see Sec. A of the Supplemental Material).

To reduce the impacts of known sources to the background estimate, we mask out relevant sky regions when calculating the background. Detected sources by LHAASO-KM2A¹ with a pre-trial significance of 5σ , and known sources from those compiled in TeVCat² [40] were masked with mask radii $R_{\text{mask}} = n \cdot \sigma$, where n is a constant factor, and $\sigma = \sqrt{\sigma_{\text{psf}}^2 + \sigma_{\text{ext}}^2}$ is the combined Gaussian width of the point spread function (PSF) of KM2A σ_{psf} and the source extension σ_{ext} . Since the PSF varies with energy, we adopt the largest one in the energy bin of 10 – 15 TeV to get consistent ROIs for all energy bins. For a clean background sky region, $n = 5$ is adopted. To avoid repeated masking of the KM2A sources and TeVCat ones, whenever the TeVCat source is located within 2σ , where σ is the Gaussian source width of the KM2A source fitted with $E > 25$ TeV, they are regarded as the same source and the KM2A parameters are used. The Galactic plane with latitude $|b| \leq 10^\circ$ for declination $\delta \leq 50^\circ$ and $|b| \leq 5^\circ$ for $\delta > 50^\circ$ was also masked. A smaller mask region for high declination regions is to ensure sufficient statistics left for an accurate background estimate.

To measure the diffuse emission, the contribution from point-like and extended sources should be excluded. Similar with above, we mask both the sources detected by KM2A and those by other experiments as compiled in TeVCat, but with

¹ The first LHAASO source catalog can be found in Ref. [39]. Here, we use each source’s fitting location, extension, and energy spectrum, assuming a two-dimensional Gaussian morphology and a power-law spectrum.

² <http://tevcat.uchicago.edu>

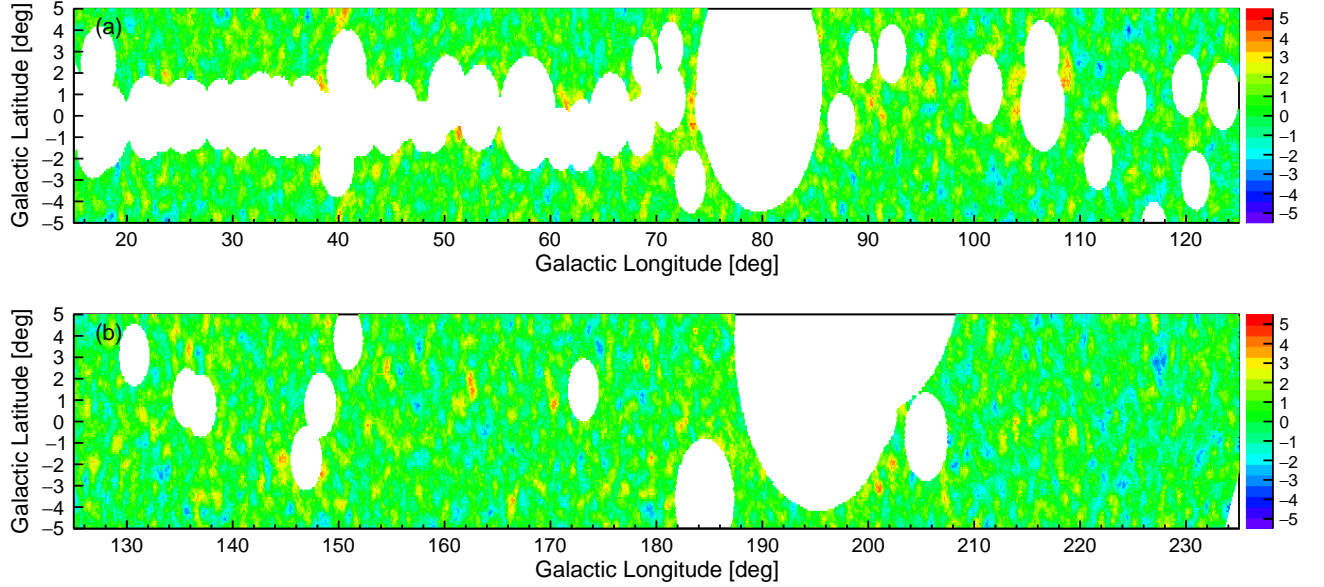


FIG. 1. The significance maps in Galactic coordinate of the inner Galaxy region (panel (a)) and outer Galaxy region (panel (b)) above 25 TeV after masking the resolved KM2A and TeVCat sources.

$n = 2.5$ to balance the source contamination and the residual sky area. Exceptions are adopted for several very extended sources, i.e., 6° for the Cygnus cocoon and 8° for Geminga and Monogem, which are slightly larger than 2.5 times of their extensions as compiled in TeVCat. Note that deviations from Gaussian profiles of these sources may exist [41].

The residual contamination of resolved sources after the masking is estimated from the morphological analysis for both the resolved sources and the diffuse emission. We employ the 2D Gaussian templates weighted by the measured fluxes for known sources. For the diffuse emission, we use the morphology of the gas distribution as traced by the PLANCK dust opacity map, assuming a uniform ratio between the dust opacity and the gas column [42]. Fitting to the observational data we can obtain the relative contributions of the diffuse component and the residual source component. The contamination of resolved sources for $n = 2.5$ is found to be smaller than 6% throughout the analyzed energy ranges, as summarized in Table S1 of the Supplemental Material. Due to

the improvement of the PSF with energy, the contamination decreases efficiently at high energies. The contamination is subtracted when calculating the fluxes of the diffuse emission.

We employ a test statistic (TS) that utilizes twice the logarithmic likelihood ratio to determine the significance of the diffuse emission. Specifically, we compute $TS = 2 \ln(\mathcal{L}_{s+b}/\mathcal{L}_b)$, where \mathcal{L}_{s+b} and \mathcal{L}_b represent the likelihoods for the signal plus background hypothesis (H_1) and the background only hypothesis (H_0), respectively. We assume a power-law model of the spectrum of the diffuse emission in the fitting, with $\phi(E)$ expressed as $\phi_0 (E/E_0)^{-\alpha}$, where $E_0 = 50$ TeV is the pivot energy. We implement a forward-folding procedure to optimize the model parameters and estimate the background from the observational data. Note that, the statistical uncertainties of the background are relatively large at high energies, which need to be properly considered in the fitting process.

The likelihood ratio is defined as

$$\frac{\mathcal{L}_{s+b}}{\mathcal{L}_b} = \frac{\prod_{i=0}^n \text{Poisson}(N_i^{\text{obs}}, N_i^{\text{sig}}(\phi_0, \alpha) + N_i^{\text{bkg},1}) \cdot \text{Gauss}(N_i^{\text{off}}; N_i^{\text{bkg},1}, \sigma_i^{\text{bkg}})}{\prod_{i=0}^n \text{Poisson}(N_i^{\text{obs}}, N_i^{\text{bkg},0}) \cdot \text{Gauss}(N_i^{\text{off}}; N_i^{\text{bkg},0}, \sigma_i^{\text{bkg}})}, \quad (1)$$

where N_i^{obs} is the observed number of counts in the ROI in the i -th energy bin, N_i^{off} is the estimated background number of counts, N_i^{sig} is the predicted number of counts obtained from folding the diffuse spectrum to the exposure and response functions (energy and angular) of the KM2A detector, $N_i^{\text{bkg},0}$

and $N_i^{\text{bkg},1}$ are predicted background numbers of counts under the hypotheses H_0 and H_1 , and σ_i^{bkg} is the statistical uncertainty of the estimated background. Note that $N_i^{\text{bkg},0}$ and $N_i^{\text{bkg},1}$ are nuisance parameters to be fitted.

To determine σ_i^{bkg} , we generate thousands of mock data sets

for each energy bin by randomly assigning the arrival time of every event in the observational data. We then apply the same background estimation technique to each mock data set, which yields a distribution of estimated background counts (N_i^{off}) for given energy bin. This distribution can be approximately described by a Gaussian distribution with width σ_i^{bkg} . The likelihood function in Eq. (1) includes a Poisson term, representing the statistical probability of the observed number of events, and a Gaussian term, representing the probability of the background fluctuation. The flux in each energy bin is determined by fitting the normalization parameter ϕ_0 , while the spectral index is fixed at the best-fit value obtained from the whole-band fitting.

Results. — The LHAASO-KM2A significance maps of the two sky regions after masking detected sources are shown in Fig. 1. The one-dimensional significance distributions are given in Fig. S2 in the Supplemental Material. As a comparison, reference regions which are ROIs shifted along the right ascension (R.A.) in the celestial coordinates show standard Gaussian distributions of the significance, indicating that our background estimate is reasonable (Fig. S2 of the Supplemental Material). The total significance of the inner (outer) Galaxy region is 29.1σ (12.7σ). No significant point-like sources are present in the significance maps after the mask, except for some hot spots, which need more data to confirm whether they are point-like sources or diffuse emissions. The LHAASO results give the first measurement of diffuse emission in the outer Galaxy region in the VHE-UHE domain.

Fig. 2 shows the derived fluxes of the diffuse emission in the two regions. The fluxes in different energy bins are tabulated in Tables S2 and S3 of the Supplemental Material. From Fig. 1 we can see that considerable regions along the innermost Galactic disk are masked for the inner Galaxy region. Since the expected diffuse emission is non-uniform, the current measurements are thus not equivalent to the total average emission in the ROIs. As an estimate, we find that the average diffuse emission in the ROIs without any masking will be higher by $\sim 61\%$ and $\sim 2\%$ than our measurements assuming a spatial template of the PLANCK dust opacity map in the inner and outer Galactic regions, respectively.

We fit the measured spectrum using a power-law function, finding that the index is $-2.99 \pm 0.04_{\text{stat}}$ for the inner Galaxy region and $-2.99 \pm 0.07_{\text{stat}}$ for the outer Galaxy region (see Table I). Possible spectral structures deviating from power-laws are not significant, and more data statistics are needed to further address such issues. As a comparison, the power-law fitting to the spectrum without subtracting the residual source contamination as given in Table S1 obtains $-3.01 \pm 0.04_{\text{stat}}$ for the inner region and $-2.99 \pm 0.07_{\text{stat}}$ for the outer region, indicating that the effect due to residuals of known sources is minor.

In Fig. 3, we present the longitude and latitude profiles for the two sky regions, for energy bands of 10 – 63 TeV and 63 – 1000 TeV. The latitude integration range when deriving the longitude profile is from -5° to $+5^\circ$, and the longitude integration ranges for the latitude profiles are the same as the definitions of the ROIs. The diffuse emission shows a clear

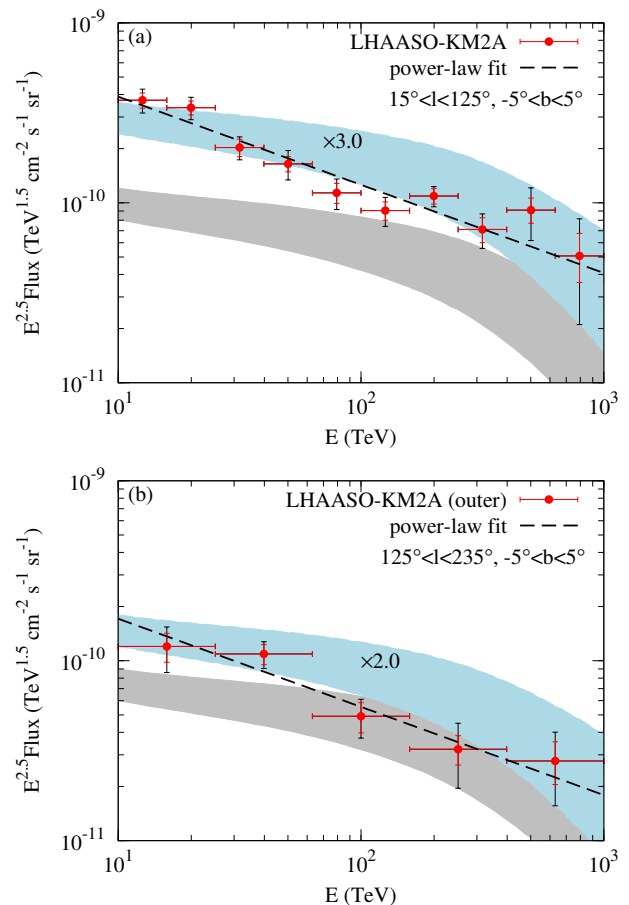


FIG. 2. Measured fluxes of diffuse γ -ray emission in the inner and outer Galaxy regions. The smaller error bars show the statistical errors and the larger ones show the quadratic sum of the statistical and systematic errors. In each panel, the dashed line shows the best-fit power-law function of the data, the grey shaded band shows the model prediction assuming local CR spectra and the gas column density with the same mask as the data, and the cyan shaded band is the grey one multiplied by a constant factor of 3.0 for the inner region and 2.0 for the outer region.

TABLE I. Fitting parameters of the LHAASO-KM2A diffuse spectra.

	ϕ_0 ($10^{-14} \text{ TeV}^{-1} \text{ cm}^{-2} \text{ s}^{-1} \text{ sr}^{-1}$)	α
Inner Galaxy	$1.00 \pm 0.04_{\text{stat}} \pm 0.09_{\text{sys}}$	$-2.99 \pm 0.04_{\text{stat}} \pm 0.07_{\text{sys}}$
Outer Galaxy	$0.44 \pm 0.04_{\text{stat}} \pm 0.05_{\text{sys}}$	$-2.99 \pm 0.07_{\text{stat}} \pm 0.12_{\text{sys}}$

decrease from the inner Galaxy to the outer Galaxy and a concentration in the low Galactic latitudes. We fit the longitude and latitude distributions using the gas template traced by the PLANCK dust opacity map, as shown by the solid line in each panel. The results show that the measured latitude distributions generally agree with the gas distribution, except for a slight deviation for 10 – 63 TeV profile in the outer region (the p -value of the fitting is about 0.03). We can see a clear deviation of the data from the gas template for the longitude

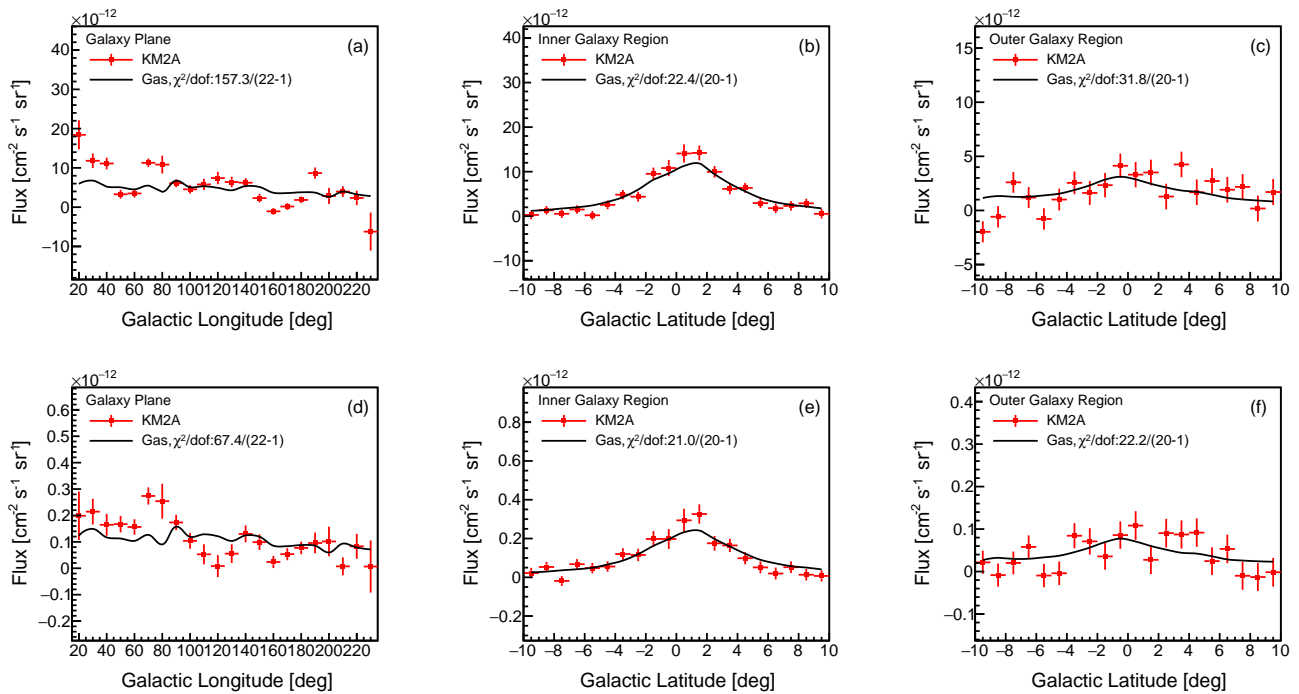


FIG. 3. Galactic longitude and latitude profiles of the diffuse emission for energy bands 10 – 63 TeV (top three panels) and 63 – 1000 TeV (bottom three panels), respectively. The solid line in each panel is the best-fit gas distribution according to the PLANCK dust opacity map.

distribution. The fitting gives $\chi^2/dof = 157.3/21$ and $67.4/21$ for 10 – 63 TeV and 63 – 1000 TeV energy bands, corresponding to p -values of about 7×10^{-23} and 10^{-6} , respectively. The results indicate that the gas distribution may not well trace the diffuse γ -ray emission at very high energies. We calculate the angular power spectrum of the relative γ -ray flux map with $E > 25$ TeV, and find that it is consistent with the angular power spectrum of the gas distribution for multipole $l > 10$ but shows slightly higher power for smaller l , which may indicate that the data are more clumpy than the gas distribution. See Fig. S3 of the Supplemental Material. We also fit the latitude profiles by adding a Gaussian latitude distribution centered at $b = 0$ to the gas template but find only slight improvements in the goodness-of-fit (see Fig. S4 of the Supplemental Material).

Systematic uncertainties. — The event rate varies during the operation due to the variation of temperature and humidity of the atmosphere, affecting the detection efficiency for γ -rays. This effect results in about 7% systematic uncertainty for the flux (ϕ_0) and 0.02 for the spectral index (α) for point-like sources [36]. For the diffuse emission in this work, we expect that the variation of atmospheric conditions contributes to similar systematic uncertainties since its main impact is on the detection efficiency. The array layout changed slightly for debugging purposes during the operation, which results in about 1% variation for ϕ_0 and 0.02 change for α , estimated from simulations with two layouts. To account for the systematic uncertainties from the background estimate method, we vary the time window for background estimate from ± 5 hours to ± 2 , ± 6 , and ± 12 hours, vary the mask maps for the back-

ground estimate (e.g., $|b| \leq 5^\circ$ for declination $\delta \leq 60^\circ$ which enables shorter time windows), and test different large-scale efficiency correction parameters, and obtain the impacts on ϕ_0 of about 5% (10%) and on α of about 0.05 (0.10), for the inner (outer) region.

The γ -ray survival fraction as a function of the γ /CR discrimination parameter $R_{\mu e}$ is obtained by Monte Carlo (MC) simulations. The difference in the survival fraction between MC and experimental data may lead to systematic uncertainties. We compared the spectra using different groups of $R_{\mu e}$, and estimated the systematic uncertainties to be about 2% (5%) for ϕ_0 and 0.04 (0.06) for α for the inner (outer) Galaxy region. By combining all these systematic uncertainties in quadrature, the overall systematic uncertainties are 9% (12%) for ϕ_0 and 0.07 (0.12) for α , for the inner (outer) region. The systematic uncertainties of the flux in each energy bin are given in Tables S2 and S3 of the Supplemental Material.

Discussion. — We compare the LHAASO measurements of diffuse emission with the predictions of hadronic interactions between CRs and the ISM. While the CR spectra were directly measured with relatively small uncertainties below ~ 100 TeV [21, 22, 43, 44], the uncertainties at higher energies are large, particularly for individual elements [45, 46]. We use the sum of two power-law functions with an exponential cutoff, $\sum_{i=1,2} A_i E^{-B_i} \exp(-E/C_i)$, to describe the local spectra of both protons and helium nuclei, and adjust the parameters A_i , B_i , C_i to give low and high fittings to the data (see Fig. S5 and Table S4 of the Supplemental Material). Assuming the CR intensity is uniform in the Galaxy as a zero-order approximation, we obtain the expected diffuse γ -ray

emission in the two regions from hadronic interactions between CR nuclei and the ISM. We assume the ISM hydrogen and helium distributions follow the PLANCK dust opacity map [42], and the number density of helium to hydrogen is 1 : 10. Heavier nuclei are expected to contribute to a fraction of $\lesssim 10\%$ of the total emission and are neglected in this work [47]. The secondary γ production spectrum is calculated using the AAfrag package [48]. We also include the $\gamma\gamma$ absorption effect³, which is important for $E > 100$ TeV [50].

The results are given by grey shaded bands in Fig. 2, with bandwidth representing the uncertainty from the CR flux measurements. It can be seen that the predicted fluxes are lower than the measured ones⁴. As a comparison, we scale the grey bands by a factor of 3 for the inner region and 2 for the outer region, as shown by the cyan shaded bands, which can roughly match with the data. The spectral shapes of the measurements are basically power-laws, which are slightly different from the predicted curved spectra. To quantify their differences, we fit the fluxes (with statistical and systematic uncertainties added in quadrature) with the predicted “high” spectral shape (with normalization free) which gives $\chi^2/dof = 33.8/9$ (7.7/4) in the inner (outer) region, and with the “low” spectral shape which gives $\chi^2/dof = 21.9/9$ (4.4/4). The p -values of the fittings are about $10^{-4} \sim 10^{-2}$ for the inner region, and $0.10 \sim 0.35$ for the outer region. As a comparison, the power-law fitting gives $\chi^2/dof = 9.1/8$ (2.2/3). For the inner region, excesses exist for the whole energy band, while for the outer region, excesses mainly appear at low energies (for $E \lesssim 60$ TeV). The LHAASO measurements may thus imply the existence of additional sources for the diffuse emission. The excesses may come from unresolved sources. Although sources above 5σ detected by KM2A and other experiments were masked from the data, there should be sources below the chosen threshold whose accumulative contribution may account for a fraction of the observed emission [26]. The ICS from electrons and positrons injected from pulsars or pulsar wind nebulae may be proper candidates [1, 18, 23, 24]. Some such sources were detected as extended halos in the VHE band [30, 41]. It is expected that such pulsar halos may be general in the Milky Way, giving remarkable diffuse emission in the VHE to UHE band [23, 24]. The imperfect correlation of the longitudinal distributions of the data with gas may support such a scenario. Alternatively, CR interactions with the medium around acceleration sources [25, 51], the spatial variations of the CR spectra (e.g., harder spectra in places other than the local vicinity; [52–54]) or dust-to-gas ratio [55] may also explain the excesses.

Conclusion.— We report the measurements of the diffuse γ -ray emission in the VHE to UHE window of 10 – 1000 TeV from the Galactic plane using the LHAASO-KM2A data. In

total, 302 days of the half array data, 219 days of the 3/4 array data, and 423 days of the full array data of LHAASO-KM2A are used in this work. To reduce the contamination from detected sources, the sky regions around known VHE/UHE sources and those newly detected by the LHAASO-KM2A are masked. In the Galactic plane, Two sky regions (Fig. 1), the inner Galaxy and the outer Galaxy regions, are analyzed. After masking the sources, we find significant diffuse emission above 10 TeV with 29.1σ and 12.7σ significance for the inner and outer Galaxy regions, respectively. The outer Galaxy region is, for the first time, to be observed to have VHE-UHE diffuse emission. A power-law can well describe the spectra in both the inner and outer regions with similar spectral indices of -2.99 . Compared with the prediction of CR interactions with the ISM, the LHAASO measured fluxes are higher by a factor of $2 \sim 3$ in both regions (for the outer region the excess is evident for $E \lesssim 60$ TeV). The latitude distributions of the diffuse emission are in general consistent with the gas distribution, while deviation is shown in the longitude distribution. The KM2A measurements provide interesting insights in probing the source distribution and interactions of CRs in the Galaxy. Further understanding of the nature of the diffuse emission is expected to be achieved with the accumulation of more data by KM2A and the analysis from sub-TeV to ~ 10 TeV energies with the WCDA data, and/or a joint modeling of the recently reported detection of neutrino emission from the Galactic plane by IceCube [56].

ACKNOWLEDGMENTS

We would like to thank all staff members who work at the LHAASO site above 4400 meters above sea level year-round to maintain the detector and keep the water recycling system, electricity power supply and other components of the experiment operating smoothly. We are grateful to Chengdu Management Committee of Tianfu New Area for the constant financial support for research with LHAASO data. This work is also supported by the following grants: the National Key R&D program of China under grants 2018YFA0404202, 2018YFA0404201, 2018YFA0404203, and 2018YFA0404204, the National Natural Science Foundation of China under grants 12220101003, 12273114, 12022502, 12205314, 12105301, 12261160362, 12105294, U1931201, the Project for Young Scientists in Basic Research of Chinese Academy of Sciences under grant YSBR-061, the Program for Innovative Talents and Entrepreneur in Jiangsu, and the NSRF of Thailand via the Program Management Unit for Human Resources & Institutional Development, Research and Innovation under grant B37G660015.

³ The absorption optical depth is a function of photon energy and travel path, and thus depends on the spatial emissivity of the γ -ray radiation. We employ the GALPROP code [2, 3] to calculate the diffuse γ -ray emissivity and implement the absorption obtained with the ISRF embedded in GALPROP, using propagation parameters determined by recent CR observations [49].

⁴ Note that the spatial inhomogeneity of CR intensity may change the prediction. As an estimate, for a GALPROP model with parameters given in Ref. [49], including the spatial distribution of CRs results in 5% (41%) lower fluxes in the inner (outer) region.

- [1] F. A. Aharonian and A. M. Atoyan, *Astron. Astrophys.* **362**, 937 (2000), astro-ph/0009009.
- [2] A. W. Strong, I. V. Moskalenko, and O. Reimer, *Astrophys. J.* **537**, 763 (2000), astro-ph/9811296.
- [3] A. W. Strong, I. V. Moskalenko, and O. Reimer, *Astrophys. J.* **613**, 962 (2004), astro-ph/0406254.
- [4] M. Ackermann, et al., *Astrophys. J.* **750**, 3 (2012).
- [5] G. W. Clark, G. P. Garmire, and W. L. Kraushaar, *Astrophys. J. Lett.* **153**, L203 (1968).
- [6] C. E. Fichtel, R. C. Hartman, D. A. Kniffen, D. J. Thompson, G. F. Bignami, H. Ögelman, M. E. Özel, and T. Tümer, *Astrophys. J.* **198**, 163 (1975).
- [7] H. A. Mayer-Hasselwander, et al., *Astron. Astrophys.* **105**, 164 (1982).
- [8] S. D. Hunter, et al., *Astrophys. J.* **481**, 205 (1997).
- [9] A. A. Abdo, et al., *Astrophys. J. Lett.* **658**, L33 (2007), astro-ph/0611691.
- [10] A. A. Abdo, et al., *Astrophys. J.* **688**, 1078 (2008), 0805.0417.
- [11] B. Bartoli, et al., *Astrophys. J.* **806**, 20 (2015), 1507.06758.
- [12] M. Amenomori, et al., *Phys. Rev. Lett.* **126**, 141101 (2021).
- [13] A. Abramowski, et al., *Phys. Rev. D* **90**, 122007 (2014), 1411.7568.
- [14] A. U. Abeysekara et al. (HAWC), *PoS ICRC2021*, 835 (2021).
- [15] R.-Y. Liu and X.-Y. Wang, *Astrophys. J. Lett.* **914**, L7 (2021), 2104.05609.
- [16] S. Koldobskiy, A. Neronov, and D. Semikoz, *Phys. Rev. D* **104**, 043010 (2021), 2105.00959.
- [17] B.-Q. Qiao, W. Liu, M.-J. Zhao, X.-J. Bi, and Y.-Q. Guo, *Frontiers of Physics* **17**, 44501 (2022), 2104.03729.
- [18] F. A. Aharonian, *Very high energy cosmic gamma radiation : a crucial window on the extreme Universe* (World Scientific Publishing, 2004).
- [19] O. Adriani, et al., *Science* **332**, 69 (2011), 1103.4055.
- [20] M. Aguilar, et al., *Phys. Rev. Lett.* **114**, 171103 (2015).
- [21] Q. An, et al., *Science Advances* **5**, eaax3793 (2019), 1909.12860.
- [22] F. Alemanno, et al., *Phys. Rev. Lett.* **126**, 201102 (2021), 2105.09073.
- [23] T. Linden and B. J. Buckman, *Phys. Rev. Lett.* **120**, 121101 (2018), 1707.01905.
- [24] V. Vecchiotti, F. Zuccarini, F. L. Villante, and G. Pagliaroli, *Astrophys. J.* **928**, 19 (2022), 2107.14584.
- [25] P.-P. Zhang, B.-Q. Qiao, Q. Yuan, S.-W. Cui, and Y.-Q. Guo, *Phys. Rev. D* **105**, 023002 (2022), 2107.08280.
- [26] C. Steppa and K. Egberts, *Astron. Astrophys.* **643**, A137 (2020), 2010.03305.
- [27] Z. Cao, et al., *Chinese Physics C* **46**, 035001 (2022), 1905.02773.
- [28] Z. Cao, et al., *Nature* **594**, 33 (2021), URL <https://doi.org/10.1038/s41586-021-03498-z>.
- [29] Z. Cao, et al., *Science* **373**, 425 (2021), URL <https://doi.org/10.1126/science.abg5137>.
- [30] F. Aharonian, et al., *Phys. Rev. Lett.* **126**, 241103 (2021), 2106.09396.
- [31] Z. Cao, et al., *Astrophys. J. Lett.* **919**, L22 (2021), 2106.09865.
- [32] Z. Cao, et al., *Astrophys. J. Lett.* **917**, L4 (2021), 2107.02020.
- [33] D. Heck, J. Knapp, J. N. Capdevielle, G. Schatz, and T. Thouw, *CORSIKA: a Monte Carlo code to simulate extensive air showers*. (TIB Hannover, 1998).
- [34] S. Chen, in *36th International Cosmic Ray Conference (ICRC2019)* (2019), vol. 36 of *International Cosmic Ray Conference*, p. 219.
- [35] S. Agostinelli, et al., *Nuclear Instruments and Methods in Physics Research A* **506**, 250 (2003).
- [36] F. Aharonian, et al., *Chinese Physics C* **45**, 025002 (2021).
- [37] K. Greisen, *Annual Review of Nuclear Science* **10**, 63 (1960).
- [38] R. Fleyscher, L. Fleyscher, P. Nemethy, A. I. Mincer, and T. J. Haines, *Astrophys. J.* **603**, 355 (2004), astro-ph/0306015.
- [39] Z. Cao, et al., arXiv e-prints arXiv:2305.17030 (2023), 2305.17030.
- [40] S. P. Wakely and D. Horan, *International Cosmic Ray Conference* **3**, 1341 (2008).
- [41] A. U. Abeysekara, et al., *Science* **358**, 911 (2017), 1711.06223.
- [42] Planck Collaboration, et al., *Astron. Astrophys.* **596**, A109 (2016), 1605.09387.
- [43] A. D. Panov, et al., *Bulletin of the Russian Academy of Science, Phys.* **73**, 564 (2009), 1101.3246.
- [44] Y. S. Yoon, et al., *Astrophys. J.* **839**, 5 (2017), 1704.02512.
- [45] W. D. Apel, et al., *Astroparticle Physics* **47**, 54 (2013).
- [46] M. G. Aartsen, et al., *Phys. Rev. D* **100**, 082002 (2019), 1906.04317.
- [47] M. Breuhaus, J. A. Hinton, V. Joshi, B. Reville, and H. Schoorlemmer, *Astron. Astrophys.* **661**, A72 (2022), 2201.03984.
- [48] M. Kachelrieß, I. V. Moskalenko, and S. Ostapchenko, *Computer Physics Communications* **245**, 106846 (2019), 1904.05129.
- [49] Q. Yuan, C.-R. Zhu, X.-J. Bi, and D.-M. Wei, *J. Cosmol. Astropart. Phys.* **2020**, 027 (2020), 1810.03141.
- [50] J.-L. Zhang, X.-J. Bi, and H.-B. Hu, *Astron. Astrophys.* **449**, 641 (2006), astro-ph/0508236.
- [51] R. Yang and F. Aharonian, *Phys. Rev. D* **100**, 063020 (2019), 1812.04364.
- [52] Y.-Q. Guo and Q. Yuan, *Phys. Rev. D* **97**, 063008 (2018), 1801.05904.
- [53] P. Lipari and S. Vernetto, *Phys. Rev. D* **98**, 043003 (2018), 1804.10116.
- [54] P. De La Torre Luque, D. Gaggero, D. Grasso, O. Fornieri, K. Egberts, C. Steppa, and C. Evoli, *Astron. Astrophys.* **672**, A58 (2023), 2203.15759.
- [55] A. Giannetti, S. Leurini, C. König, J. S. Urquhart, T. Pillai, J. Brand, J. Kauffmann, F. Wyrowski, and K. M. Menten, *Astron. Astrophys.* **606**, L12 (2017), 1710.05721.
- [56] IceCube Collaboration, R. Abbasi, M. Ackermann, J. Adams, J. A. Aguilar, M. Ahlers, M. Ahrens, J. M. Alameddine, A. A. Alves, et al., *Science* **380**, 1338 (2023).

SUPPLEMENTAL MATERIAL

A. Correction of large-scale structures

The “direct integration method” of the background estimate may introduce large-scale structures using events within a relatively long time window (10 hours), which need to be corrected. The possible origin of such structures can be attributed to two causes: the true large-scale anisotropy of γ -like CR events and the spurious anisotropy due to variations in the spatial distribution of the efficiency over the time window. To correct the large-scale structures, we smooth the ON and OFF counts map (with known sources and the Galactic plane, $|b| \leq 10^\circ$ for declination $\delta \leq 50^\circ$ and $|b| \leq 5^\circ$ for $\delta > 50^\circ$, masked) with 20° radius top-hat kernel, and then correct the estimated background by multiplying $N_{\text{on}}/N_{\text{off}}$ of each pixel obtained after the smoothing. The resulting significance map shows no such large-scale structures any more, as shown in Fig. S1. Different smoothing window sizes are tested, and the changes of the results are taken as systematic uncertainties.

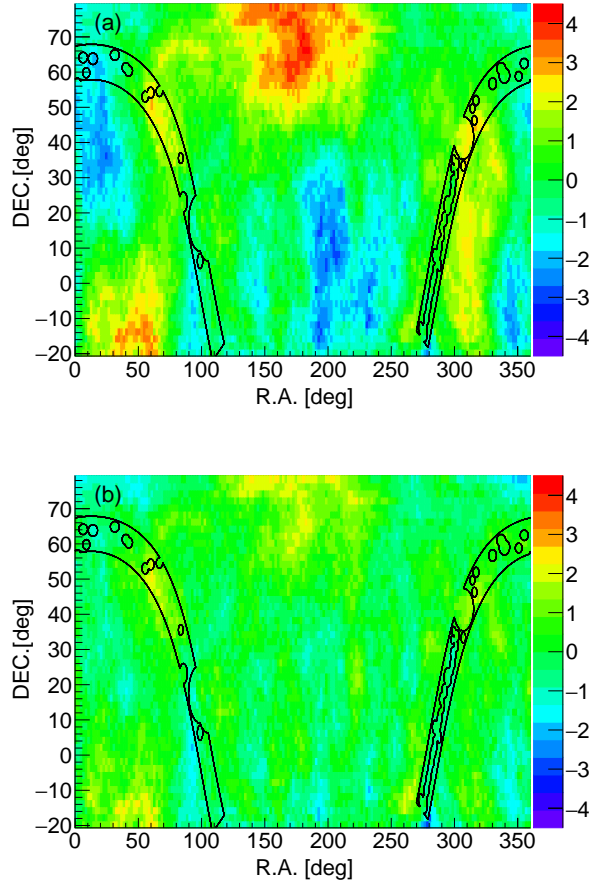


FIG. S1. Significance maps in celestial coordinate for energy bin of 10 – 15 TeV for the KM2A full array data. Panel (a) and (b) represent the results before and after the large-scale structure correction, respectively. The black solid lines show the ROIs of this analysis.

B. Residual fractions from resolved sources

Table S1 gives the calculated residual fractions of the signal that is from resolved sources, due to the tails of the extension of sources. In this work, the source residuals have been subtracted from the signal to obtain the diffuse emission fluxes.

TABLE S1. Percentage contribution of resolved sources to the total signal.

$\log(E_{\text{rec}}/\text{TeV})$	Inner Galaxy (%)	Outer Galaxy (%)
1.0-1.2	5.97 ± 0.67	4.58 ± 1.63
1.2-1.4	4.26 ± 0.43	2.25 ± 0.44
1.4-1.6	2.97 ± 0.36	1.39 ± 0.23
1.6-1.8	1.95 ± 0.21	1.88 ± 0.45
1.8-2.0	1.97 ± 0.27	0.77 ± 0.16
> 2.0	0.76 ± 0.06	0.39 ± 0.09

C. One-dimensional distributions of ROIs and control regions

Fig. S2 shows the one-dimensional significance distributions of our analyzed ROIs (top two panels) and the control sky regions with ROIs shifted along the R.A. for -30° and $+30^\circ$. For our ROIs, we see that the mean values are positive, suggesting the existence of diffuse emission in these regions. The significance distributions of the control regions are consistent with the standard Gaussian distribution expected for the background distribution.

D. Fluxes of diffuse emission measured by LHAASO-KM2A

Tables S2 and S3 present the fluxes of the diffuse emission in the inner and outer Galaxy regions measured by KM2A, with 1σ statistical errors and the estimated systematic uncertainties.

TABLE S2. Fluxes with 1σ statistical uncertainties and systematic uncertainties of the diffuse emission in the inner Galaxy region measured by KM2A.

$\log(E_{\text{rec}}/\text{TeV})$	$\langle E \rangle$ (TeV)	$\phi \pm \sigma_{\text{stat}} \pm \sigma_{\text{sys}}$ ($\text{TeV}^{-1} \text{cm}^{-2} \text{s}^{-1} \text{sr}^{-1}$)
1.0-1.2	12.6	$(6.61 \pm 0.64 \pm 0.77) \times 10^{-13}$
1.2-1.4	20.0	$(1.90 \pm 0.17 \pm 0.21) \times 10^{-13}$
1.4-1.6	31.6	$(3.61 \pm 0.40 \pm 0.34) \times 10^{-14}$
1.6-1.8	50.1	$(9.26 \pm 0.90 \pm 1.47) \times 10^{-15}$
1.8-2.0	79.4	$(2.02 \pm 0.26 \pm 0.29) \times 10^{-15}$
2.0-2.2	125.9	$(5.09^{+0.60}_{-0.59} \pm 0.72) \times 10^{-16}$
2.2-2.4	199.5	$(1.94^{+0.19}_{-0.19} \pm 0.16) \times 10^{-16}$
2.4-2.6	316.2	$(4.00^{+0.64}_{-0.62} \pm 0.60) \times 10^{-17}$
2.6-2.8	501.2	$(1.62^{+0.27}_{-0.25} \pm 0.46) \times 10^{-17}$
2.8-3.0	794.3	$(2.85^{+0.95}_{-0.82} \pm 1.45) \times 10^{-18}$

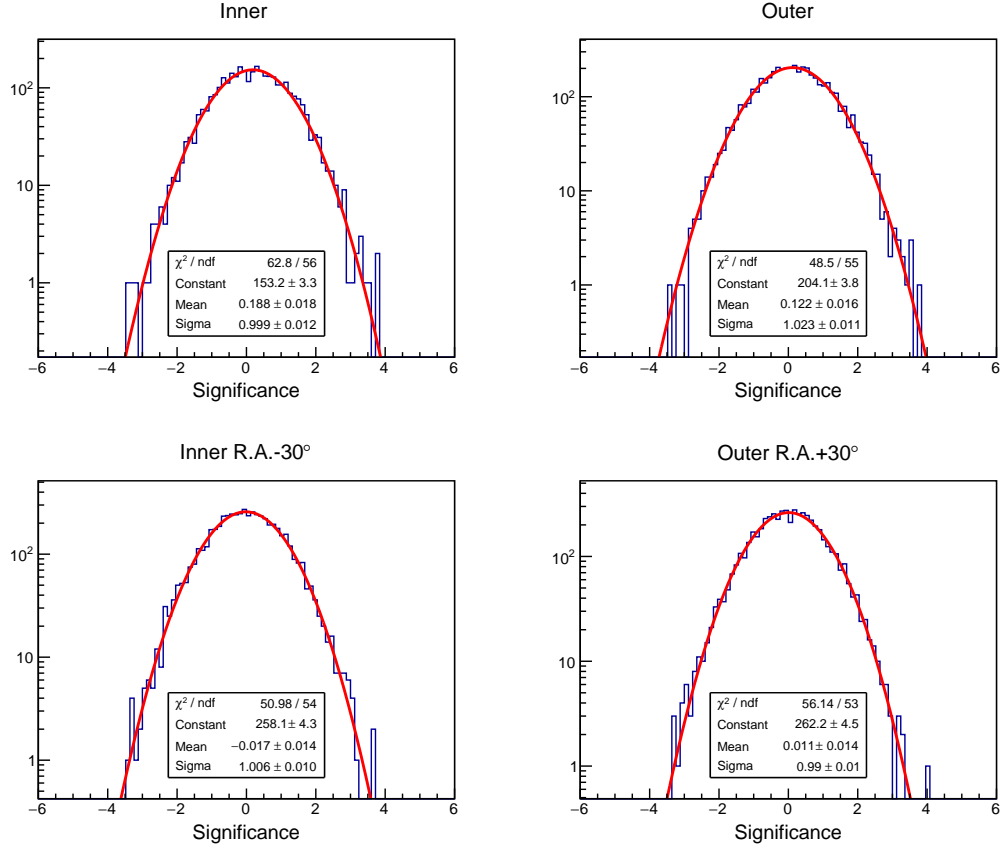


FIG. S2. One-dimensional significance distributions above 25 TeV after source masks. The pixel size is $0.5^\circ \times 0.5^\circ$. Top two panels are for our ROIs, and bottom panels are the reference sky regions shifted to lower R.A. by 30 degrees for the inner Galaxy region and higher R.A. by 30 degrees for the outer Galaxy region.

TABLE S3. Fluxes with 1σ statistical uncertainties and systematic uncertainties of the diffuse emission in the outer Galaxy region measured by KM2A.

$\log(E_{\text{rec}}/\text{TeV})$	$\langle E \rangle$ (TeV)	$\phi \pm \sigma_{\text{stat}} \pm \sigma_{\text{sys}}$ ($\text{TeV}^{-1} \text{cm}^{-2} \text{s}^{-1} \text{sr}^{-1}$)
1.0-1.4	15.8	$(1.20 \pm 0.22 \pm 0.26) \times 10^{-13}$
1.4-1.8	39.8	$(1.09 \pm 0.14 \pm 0.12) \times 10^{-14}$
1.8-2.2	100.0	$(4.91 \pm 0.94 \pm 0.74) \times 10^{-16}$
2.2-2.6	251.2	$(3.22^{+0.61}_{-0.59} \pm 1.12) \times 10^{-17}$
2.6-3.0	631.0	$(2.77^{+0.77}_{-0.72} \pm 0.97) \times 10^{-18}$

E. Angular power spectrum

The angular power spectrum can be used to statistically compare the distributions of different skymaps. The results of the angular power spectra of the relative γ -ray flux map ($E > 25$ TeV; black line), $(F - \bar{F})/\bar{F}$ where F is the flux in each pixel and \bar{F} is the average flux in the ROI, and the relative gas distribution derived from the Planck dust opacity (purple line), after applying the same mask as used in this analysis, are shown in Fig. S3. The gray band represents the 1σ statistical

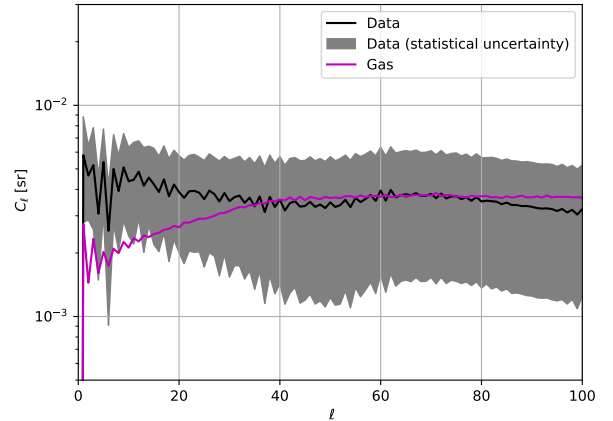


FIG. S3. Angular power spectra of the data (black) and the 1σ uncertainty band (gray shaded band), compared with the expectation based on the PLANCK-derived gas distribution (purple). The same mask as Fig. 1 is adopted when calculating the power spectra.

fluctuations of the data. The gas term is normalized to en-

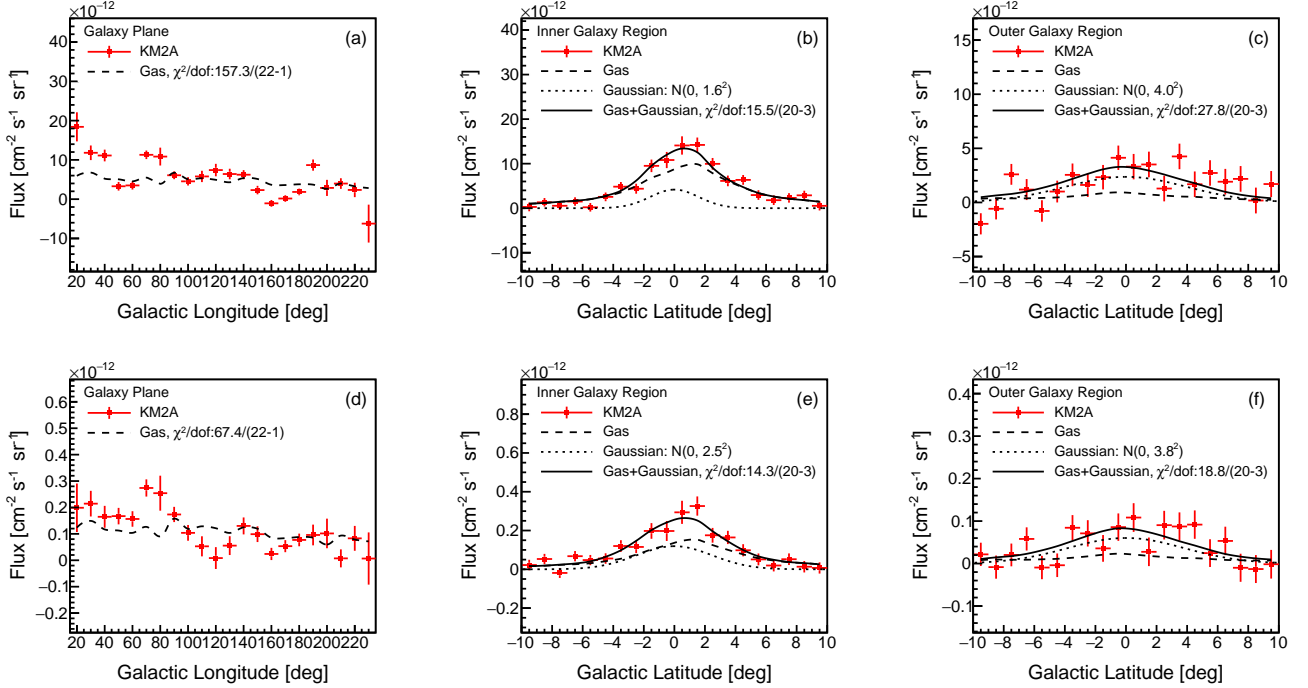


FIG. S4. Galactic longitude and latitude profiles of the diffuse emission for energy bands 10 – 63 TeV (top three panels) and 63 – 1000 TeV (bottom three panels), respectively. When fitting the diffuse emission to a combination of the PLANCK-derived gas template and a Gaussian distribution along Galactic latitude, the dashed, dotted, and solid lines in panels (b), (c), (e), and (f) are contributions from the PLANCK-derived gas template, the Gaussian distribution, and their sum, respectively. For panels (a) and (d), only the gas-related component is shown. The latitude distributions are not substantially different from those when attributing all the diffuse emission to the PLANCK-derived gas template, as in the analysis presented in the main text.

sure that the expected number of counts after convolving the LHAASO instrument response and exposure is the same as the data. Due to the limited data statistics, the fluctuation may affect the calculation of the angular power spectrum of the gas term. We thus sample 10^3 times according to Poisson distributions and derive the median value as represented by the purple line. It is shown that for $l > 10$ the current data give consistent angular power spectrum with the expectation based on the gas model. At smaller l , the data give slightly higher power than the gas model, which indicates that the data are more clumpy than the gas distribution. This is in general agreement with the one-dimensional longitude distribution (Fig. 3). However, the differences under the current statistics are small. With the accumulation of data, further exploration along this regard is necessary.

F. Longitude and latitude distributions for alternative fittings

The PLANCK gas distribution is employed as template to fit the longitude and latitude distributions in the main text. To study possible contributions to the diffuse emission from components other than that proportional to the gas column density,

we add a Gaussian template along Galactic latitudes to the fittings. Fig. S4 shows the longitude and latitude distributions overplotted with the fitting results. The inclusion of a Gaussian template does improve the fitting slightly, compared to attributing all the diffuse emission to the PLANCK-derived gas template. However, the difference is not significant enough to claim the detection of a new component with morphology different from the gas-related component.

G. Local CR spectral fittings

Fig. S5 shows the proton and helium spectra measured locally by balloon or space experiments [21, 22, 43, 44] and ground-based air shower experiments [45, 46]. We use the sum of two exponentially cutoff power-law functions

$$A_1(E/\text{TeV})^{-B_1} \exp(-E/C_1) + A_2(E/\text{TeV})^{-B_2} \exp(-E/C_2),$$

to fit the data. The parameters (Table S4) are adjusted to properly reflect the uncertainties of the measurements. The resulting high and low representations of the CR spectra are shown by the solid and dashed lines, respectively.

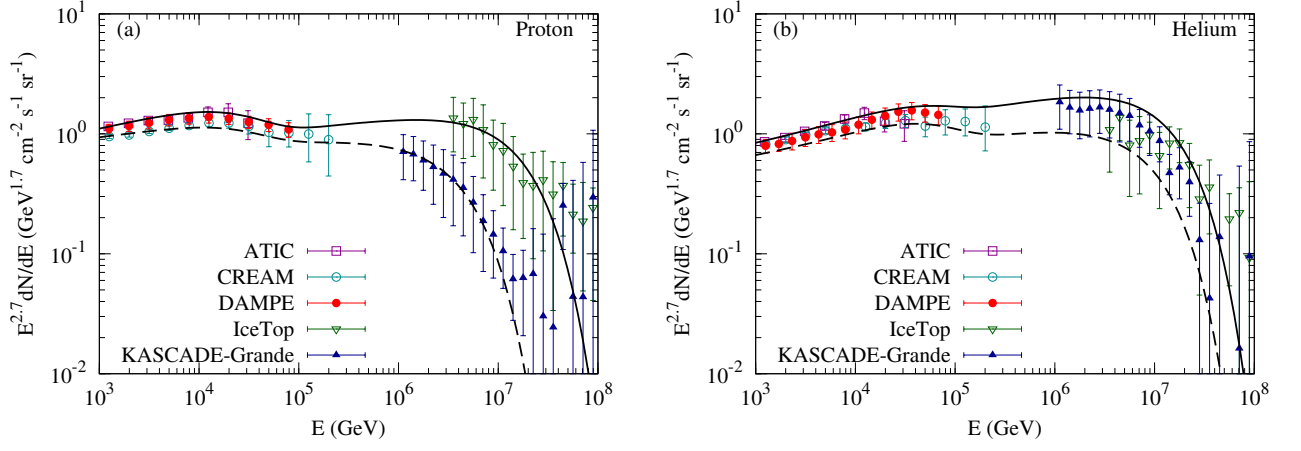


FIG. S5. Spectra of locally measured protons (a) and helium (b) together with phenomenological fittings to represent the uncertainties.

TABLE S4. Fitting parameters of the local CR spectra.

	A_1	B_1	C_1	A_2	B_2	C_2
	$\text{GeV}^{-1}\text{cm}^{-2}\text{s}^{-1}\text{sr}^{-1}$		TeV	$\text{GeV}^{-1}\text{cm}^{-2}\text{s}^{-1}\text{sr}^{-1}$		PeV
Proton-High	3.40×10^{-9}	2.35	25.0	5.51×10^{-9}	2.60	15.0
Proton-Low	1.80×10^{-9}	2.35	25.0	5.71×10^{-9}	2.66	4.0
Helium-High	0.75×10^{-9}	2.10	50.0	5.95×10^{-9}	2.55	13.0
Helium-Low	0.75×10^{-9}	2.10	50.0	4.55×10^{-9}	2.60	9.0